Supplementary Materials

Remote spin-state engineering of Fe_2Ni clusters via graphdiyne-MXene heterointerface for boosted N_2 reduction

Dan Zhang,[a] Xiaonan Wei,[a] Junfei Ding,[a] Shucheng Liu,[a] Yanli Chen,[a] Zhimei Sun[b] and Qiong Peng*[a]

[a.] College of Physics, Guizhou University, Guiyang 550025, China

[b.] School of Materials Science and Engineering, Beihang University, Beijing 100191, China

E-mail: qpeng@gzu.edu.cn

Contents

S1. Model construction and computational details

S1.1 Density functional theory calculations

All spin-polarised density functional theory (DFT) calculations were implemented in the Vienna *ab initio* simulation package (VASP).[1] The exchange-correlation interaction was described using the Perdew-Burke-Ernzerhof (PBE) functional within the generalized gradient approximation (GGA).[2] To deal with the weak interactions between the catalyst and $*N_xH_y$ reaction intermediates, the DFT-D3 semiempirical scheme was used for all the calculations.[3] In the self-consistent field (SCF) iteration process, the convergence criteria for force and energy are set to 0.02 eV/Å and 10^{-5} eV, respectively. To validate the computational parameters, convergence tests for the cutoff energy and k-point sampling were performed by taking $Fe_2Ni/Mo_2TiC_2O_2$ as a case study. The total energy converges gradually with increasing plane-wave cutoff energy, and the energy variation becomes negligible when the cutoff energy exceeds 500 eV [Fig. S1(a)]. Similarly, as illustrated in Fig. S1(b), the total energy shows minimal variation with further refinement of the k-point mesh beyond 3 × 3 × 1. Based on these tests, a cutoff energy of 500 eV and a 3 × 3 × 1 Monkhorst-Pack k-point grid were employed for all calculations.

Pristine $Mo_2TiC_2O_2$ MXene has a two-dimensional hexagonal crystal structure, consisting of seven atomic layers stacked in the sequence O-Mo-C-Ti-C-Mo-O. Its optimized lattice constant a is 2.93 Å with a layer thickness h of 7.61 Å, which are in excellent agreement with reported values (a = 2.94 Å, h = 7.59 Å).[4] A 3 × 3 × 1 supercell of $Mo_2TiC_2O_2$ was constructed to act as a catalyst substrate with a 35 Å vacuum layer along the z-direction to eliminate spurious interlayer interactions. To create an active anchoring site, one surface oxygen atom was removed, forming an oxygen vacancy that stabilizes a triatomic Fe_2Ni cluster. Subsequently, a hexagonal graphdiyne (GDY) monolayer was

stacked under the $Fe_2Ni/Mo_2TiC_2O_2$ slab to form the $Fe_2Ni/Mo_2TiC_2O_2$/GDY heterostructure. The optimized lattice parameters *a* of the heterostructure is 8.77 Å. *Ab initio* molecular dynamics (AIMD) simulations[5] were performed to assess the kinetic stability of $Fe_2Ni/Mo_2TiC_2O_2$ at 300 K for 10 ps with a 2 fs time step using a Nosé thermostat.

Bader charge analysis and charge density difference calculations were carried out to quantify charge transfer among the Fe_2Ni cluster, the support, and adsorbed $*N_xH_y$ intermediates. Bonding and antibonding interactions were analyzed via the crystal orbital Hamilton population (COHP) and its integral (ICOHP) using the LOBSTER package.[6] More negative ICOHP values indicate stronger bonding strength.

S1.2 Ground-state magnetic configuration and electron localization function

To rigorously determine the ground-state magnetic configuration of $Fe_2Ni/Mo_2TiC_2O_2$/GDY, we constructed and optimized multiple spin states and magnetic orderings, including ferromagnetic (FM) and several antiferromagnetic (AFM) configurations. Table S1 shows that the FM configuration is energetically preferred, exhibiting the most negative total energy. It is therefore identified as the most stable magnetic state. Local magnetic moments are 3.154 μ_B (Fe_1), 3.086 μ_B (Fe_2), and 0.653 μ_B (Ni). Different initial FM spin states converge to the same ground state. All subsequent calculations were based on this ground-state structure.

S1.3 N_2 adsorption configuration and adsorption energy

The Gibbs free energy (ΔG_{*N_2}) of N_2 adsorption on the catalyst surface was calculated as,

$$\Delta G_{*N_2} = E_{*N_2} - E_{N_2} - E_{\text{catalyst}} + \Delta E_{\text{ZPE}} - T\Delta S \,, \tag{S1}$$

where E_{*N_2}, E_{N_2} and E_{catalyst} denote the total energies of the N_2 adsorbed catalyst, gas-phase N_2, and bare catalyst, respectively. ΔE_{ZPE} and ΔS is the change in the zero-point energy and entropy at T = 298.15 K. N_2 adsorption was examined on single-atom sites (Fe_1, Fe_2, and Ni), dual-atom sites (Fe_1-Fe_2, Fe_1-Ni, Fe_2-Ni), and the tri-atom Fe_2Ni site, considering multiple adsorption configurations including end-on, bridge, and side-on modes. As shown in Table S2, the Fe_2Ni tri-atom site exhibits the strongest N_2 adsorption with ΔG_{*N_2} = –0.350 eV in a side-on configuration, indicating that this site is the most favorable for N_2 activation.

S1.4 The d-band centre

The d-band centre (ε_d) of Fe_2Ni sites was calculated:

$$\varepsilon_d = \frac{\int_{-\infty}^{\infty} n_d(\varepsilon)\varepsilon \mathrm{d}\varepsilon}{\int_{-\infty}^{\infty} n_d(\varepsilon)\mathrm{d}\varepsilon} \tag{S2}$$

where ε denotes the energy and $n_d(\varepsilon)$ represents the electron density. As summarized in Table S3, GDY coupling triggers a notable upward shift of the averaged ε_d at Fe_2Ni sites from −2.96 eV to −1.97 eV. According to the d-band theory, a higher d-band centre generally leads to stronger adsorption of reactants. Indeed, $Fe_2Ni/Mo_2TiC_2O_2$/GDY catalyst delivers significantly enhanced N_2 adsorption (more negative adsorption free energy −1.70 eV vs. −0.35 eV) compared to the GDY-free counterpart, indicating strengthened metal-adsorbate interactions.

S1.5 The calculations of Gibbs free energy and limiting potential

In acidic media, the overall nitrogen reduction reaction (NRR) to NH_3 proceeds as,

$$N_2 + 6H^+ + 6e^- \rightleftharpoons 2NH_3, \quad \text{(S3)}$$

Depending on the adsorption configuration of N_2 (end-on or side-on), NRR may proceed via distal, alternating, enzymatic, or consecutive pathways.[7] End-on adsorbed N_2 favors distal or alternating mechanisms, whereas side-on adsorption leads to enzymatic or consecutive pathways. Regardless of the mechanism, six proton–electron transfer steps are involved.[8]

The Gibbs free energy change (ΔG) for each elementary step was computed as:[9]

$$\Delta G = \Delta E + \Delta E_{ZPE} - T\Delta S - neU + \Delta G_{pH}, \quad \text{(S4)}$$

where ΔE is the adsorption energy of N-containing intermediates due to the reaction, obtained from DFT calculations. ΔE_{ZPE} is the change in the zero-point energy. T is the temperature (T = 298.15 K). ΔS is the entropy change. U is the applied electrode potential. ΔG_{pH} is the free energy correction of pH, which can be calculated by $G_{pH} = 2.303 \times k_B T \times \text{pH}$, where k_B is the Boltzmann constant. Under vacuum conditions, the free energy is calculated at 0 V and pH of 0.

The elementary step with the largest positive ΔG is defined as the potential-determining step (PDS). The limiting potential (U_L), a key descriptor of intrinsic NRR activity, was determined by

$$U_L = -\Delta G_{max} / e, \quad \text{(S5)}$$

where ΔG_{max} denotes the most positive Gibbs free-energy change of all the elementary steps.[10]

S1.6 Constant-potential implicit solvation model

A constant-potential implicit solvation model (CP-ISM) was employed to simulate realistic electrochemical reaction environments, as implemented in the VASPsol code.[11, 12] The aqueous

electrolyte was treated as a continuum with a relative permittivity of 80.[13] The cavitation energy contribution was neglected by setting the effective surface tension parameter to 0, following standard practice in implicit solvent calculations. In addition, a linearized Poisson-Boltzmann model with a Debye length of 3.04 Å was used to describe the compensating charge in electrolyte.[14]

To probe potential-dependent reaction energetics, excess charges (Δq) ranging from −2.0 to +2.0 e, in increments of 0.4 e, were applied to the simulation cell. The potential-dependent electrochemical energy at the electrode-electrolyte interface is expressed as[15]

$$E_{\mathrm{q}} = E_{\mathrm{DFT}} - E_{\mathrm{F}}\Delta q\,, \tag{S6}$$

where E_{DFT} and E_{F} refer to the total energy and Fermi energy obtained from VASPsol calculations. The Fermi energy E_{F} and the corresponding electrode potential U (V/SHE), referenced to the standard hydrogen electrode (SHE), satisfy the following relation:[16]

$$U(\mathrm{V/SHE}) = -4.44\mathrm{V} - (E_{\mathrm{F}} + E_{\mathrm{Fermi\text{-}shift}})/e\,, \tag{S7}$$

where $E_{\mathrm{Fermi\text{-}shift}}$ denotes the Fermi energy shift correction obtained from the VASPsol.[17] The resulting energy-potential dependence follows a quadratic form:[18]

$$E(U_{\mathrm{q}}) = -\frac{1}{2}C(U_{\mathrm{q}} - U_{\mathrm{PZC}})^2 + E_{\mathrm{PZC}}\,, \tag{S8}$$

where C, U_{PZC}, and E_{PZC} correspond to the fitted values of system's capacitance, the potential of zero charge (PZC), and the energy at the PZC, respectively. For a constant potential referenced to the reversible hydrogen electrode (RHE), pH-induced shifts relative to SHE are described by[18]

$$U_{\mathrm{RHE}} = U_{\mathrm{SHE}} + 0.059 \times \mathrm{pH}\,, \tag{S9}$$

S2. Supplementary tables

Table S1. Total energies and local magnetic moments of different magnetic configurations for the $Fe_2Ni/Mo_2TiC_2O_2$/GDY system.

magnetic configurations	Fe_1		Fe_2		Ni		Total energy (eV)
	spin state	mag	spin state	mag	spin state	mag	
FM	↑	**3.154**	↑	**3.086**	↑	**0.653**	**–760.259**
AFM1	↑	3.017	↓	–2.985	↑	0.019	–759.876
AFM2	↑	3.052	↓	–2.957	↓	0.09	–759.855
AFM3	↓	–2.851	↑	3.116	↑	0.317	–759.495
AFM4	↓	–3.199	↑	2.757	↓	–0.488	–759.273

Table S2. N_2 adsorption configuration and Gibbs free energy (ΔG_{*N_2}, eV) on different sites of $Fe_2Ni/Mo_2TiC_2O_2$.

Site	Fe_1	Fe_2	Ni	Fe_1-Fe_2	Fe_1-Ni	Fe_2-Ni	Fe_2Ni
Configuration	end-on	end-on	end-on	bridge	bridge	bridge	**side-on**
							
ΔG_{*N_2}	–0.326	–0.321	–0.310	–0.290	–0.236	–0.224	**–0.350**

Table S3. The d-band centre (ε_d, eV) of Fe_2Ni sites in N_2 adsorbed $Fe_2Ni/Mo_2TiC_2O_2$ without and with GDY, together with corresponding Gibbs free energy of N_2 adsorption (ΔG_{*N_2}, eV). The ε_d values are averaged over spin-up and spin-down states.

System	ε_d				ΔG_{*N_2}
	Fe_1	Fe_2	Ni	Fe_2Ni	
w/o GDY	−2.65	−2.40	−3.25	−2.96	−0.35
w/ GDY	−1.92	−2.02	−1.87	−1.97	−1.70

To clarify the influence of the Hubbard U correction, we performed additional calculations using the PBE+U method. The Fe and Ni 3d electrons were treated with U-J values of 3.29 and 3.40 eV,

respectively, following Xu *et al.*[19] As shown in Table S4, the adsorption strength of $*N_2$ and $*N_2H$ on $Fe_2Ni/Mo_2TiC_2O_2$ and $Fe_2Ni/Mo_2TiC_2O_2$/GDY are enhanced under the PBE+U framework. Specifically, the ΔG_{*N_2} of $*N_2$ adsorption on $Fe_2Ni/Mo_2TiC_2O_2$ decreases from 0.15 to −0.25 eV, while the ΔG_{*N_2H} of $*N_2H$ adsorption decreases from 0.20 to −0.01 eV. Importantly, the GDY-supported system still exhibits more favourable N_2 activation (ΔG_{*N_2} = –0.50 eV) and hydrogenation behavior ($*N_2H$ formation, ΔG_{*N_2H} = –0.21 eV). These results demonstrate that while the Hubbard U correction modifies absolute energetics, the NRR activity trends of the catalysts remain unaffected.

Table S4. Comparison of Gibbs free energy changes (ΔG) for key $*N_2$, $*N_2H$ intermediate adsorption, and $\Delta G_{*N_2 \rightarrow *N_2H}$ for the first hydrogenation step calculated using PBE and PBE+U methods.

System	Method	ΔG_{*N_2}	ΔG_{*N_2H}	$\Delta G_{*N_2 \rightarrow *N_2H}$
$Fe_2Ni/Mo_2TiC_2O_2$	PBE	0.15	0.20	0.05
	PBE+U	–0.25	–0.01	0.24
$Fe_2Ni/Mo_2TiC_2O_2$/GDY	PBE	–0.17	0.01	0.17
	PBE+U	–0.50	–0.21	0.29

Table S5. NRR limiting potentials of $Fe_2Ni/Mo_2TiC_2O_2$/GDY under different conditions.

Condition	Vacuum	Implicit solvation	Explicit solvation	Implicit-Explicit
Limiting potential (V)	−0.44	−0.17	−0.28	−0.14

Table S6. Fitted parameters of the quadratic function of the potential and energy in the form of $E=I+b_1U+b_2U^2$. Here, I denotes the energy intercept at zero applied potential, while b_1 and b_2 represent the first- and second-order potential response coefficients, respectively. U_{PZC} (V/SHE) and C (e/V) are the potential of zero charge (PZC) and capacitance of the corresponding system, and E_{PZC} (eV) is the energy of the system at the PZC. In fitting analysis, R^2 refers to the coefficient of determination.

Species	I	b_1	b_2	C	U_{PZC}	E_{PZC}	R^2
*	–761.215	–0.236	–0.706	1.412	–0.167	–761.195	0.9991
*N_2	–778.377	0.315	–0.557	1.114	0.283	–778.332	0.9945
*NNH	–781.999	0.0720	–0.543	1.086	0.066	–781.997	0.9954
*NNH_2	–785.770	–0.148	–0.554	1.108	–0.134	–785.760	0.9987
*N	–769.961	0.255	–0.558	1.116	0.228	–769.932	0.9947
*NH	–774.310	0.274	–0.019	0.038	0.247	–773.343	0.9887
*NH_2	–778.330	–0.108	–0.529	1.058	–0.102	–778.324	0.9977
*NH_3	–782.147	–0.586	–0.529	1.058	–0.554	–781.985	0.8131
*NHNH	–786.036	–0.187	–0.541	1.082	–0.173	–786.019	0.9962
*$NHNH_2$	–790.045	–0.310	–0.494	0.988	–0.313	–789.996	0.9987
*NH_2NH_2	–795.271	–0.051	–0.514	1.028	–0.050	–795.269	0.9915

S3. Supplementary figures

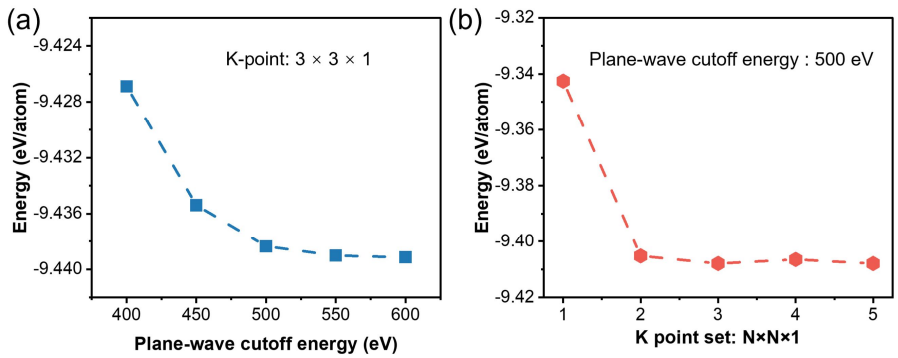

Fig. S1. Convergence tests of the average atomic energy with respect to (a) plane-wave cutoff energy and (b) k-point sampling for $Fe_2Ni/Mo_2TiC_2O_2$.

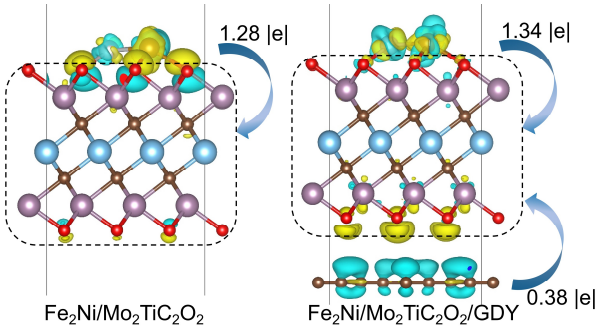

Fig. S2. Charge transfer analysis for $Fe_2Ni/Mo_2TiC_2O_2$ without and with GDY. Yellow and cyan regions represent charge accumulation and depletion, respectively.

The electron localization function (ELF) in Fig. S3 reveal more pronounced electron localization features in the GDY-supported system compared to the GDY-free counterpart, indicating a significant reorganization of the local electronic environment around the Fe_2Ni site. This enhanced localization originates from the strong electronic coupling at the GDY-MXene interface.

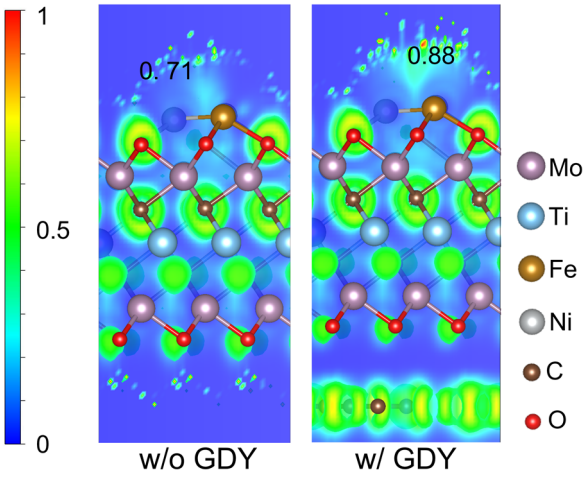

Fig. S3. Electron localization function (ELF) maps of $Fe_2Ni/Mo_2TiC_2O_2$ without and with GDY.

Although the Gibbs free energy of N_2 adsorption (ΔG_{*N2}) on $Fe_3/Mo_2TiC_2O_2$ and $Fe_2Ni/Mo_2TiC_2O_2$ is negative under vacuum condition (Fig. S4), it becomes positive ($\Delta G_{*N2} > 0$ eV) when implicit solvation is included (Fig. 2(c) and Fig. S5), indicating an endothermic and thermodynamically unfavorable adsorption process. Notably, $Fe_2Ni/Mo_2TiC_2O_2$/GDY maintains a ΔG_{*N2} under both vacuum and solvated conditions, underscoring the necessity of including realistic solvation effects.

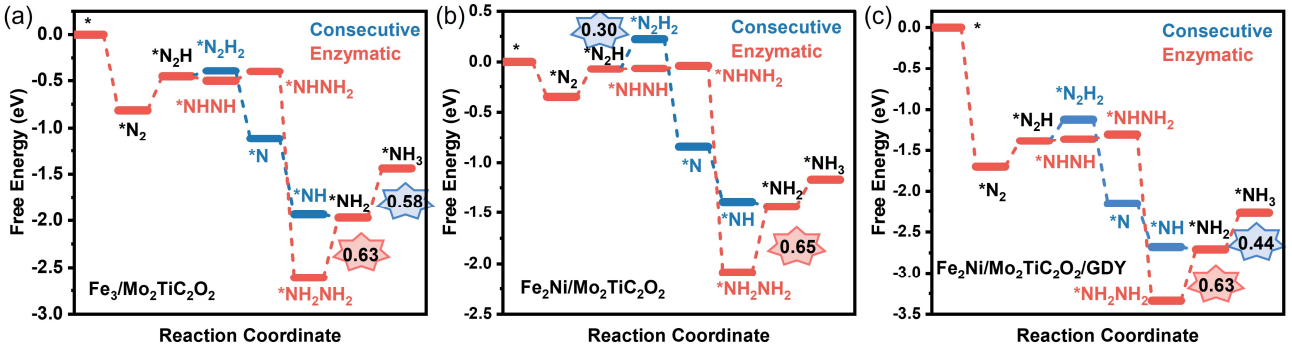

Fig. S4. Free energy profiles of the consecutive and enzymatic mechanisms on (a) $Fe_3/Mo_2TiC_2O_2$, (b) $Fe_2Ni/Mo_2TiC_2O_2$, and (c) $Fe_2Ni/Mo_2TiC_2O_2$/GDY, calculated using the constant charge model under vacuum condition.

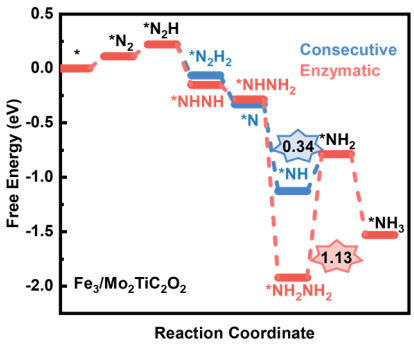

Fig. S5. The Gibbs free energy diagrams of $Fe_3/Mo_2TiC_2O_2$ using implicit solvation model.

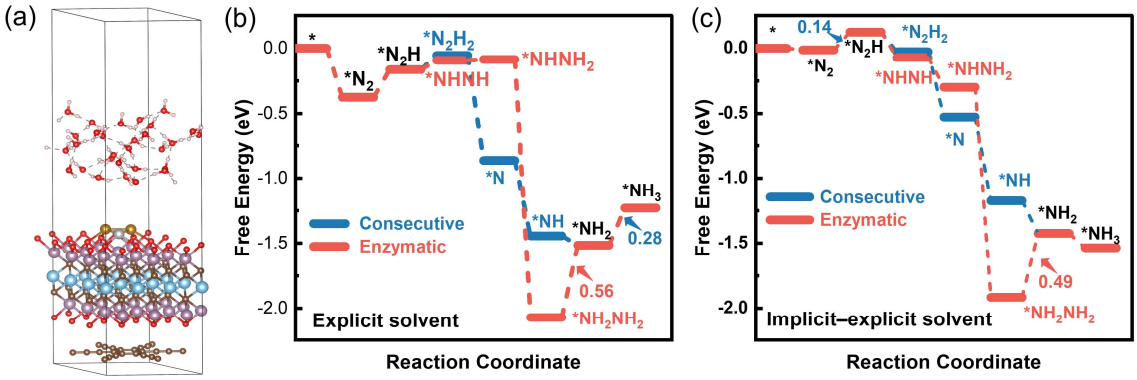

Fig. S6. (a) Explicit solvation model of $Fe_2Ni/Mo_2TiC_2O_2/GDY$. The Gibbs free energy diagrams of $Fe_2Ni/Mo_2TiC_2O_2/GDY$ using (b) explicit and (c) implicit-explicit solvation model.

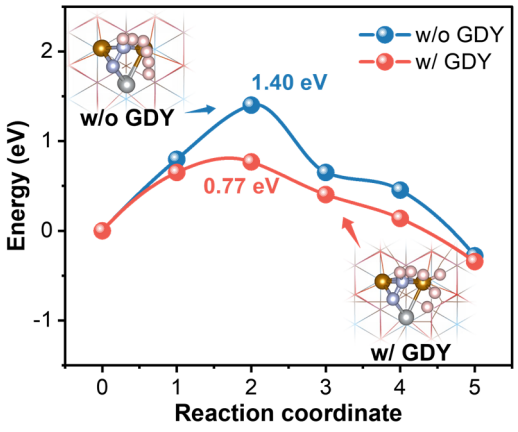

Fig. S7. Activation energy profiles for the potential-determining step ($*N_2 \rightarrow *N_2H$) on $Fe_2Ni/Mo_2TiC_2O_2$ (blue) and $Fe_2Ni/Mo_2TiC_2O_2/GDY$ (red).

Fig. S8 shows the contributions of s, p, and d orbitals for N_2 adsorption on Fe_2Ni sites. It is seen that the electronic states of Fe_2Ni active sites near the Fermi level are predominantly governed by the d orbitals rather than s and p orbitals, which controls the N_2 adsorption strength. Noted that the incorporated GDY leads to a more pronounced hybridization between Fe_2Ni d orbitals and N p orbitals near the Fermi level, indicating enhanced N_2 absorption and N≡N bond activation.

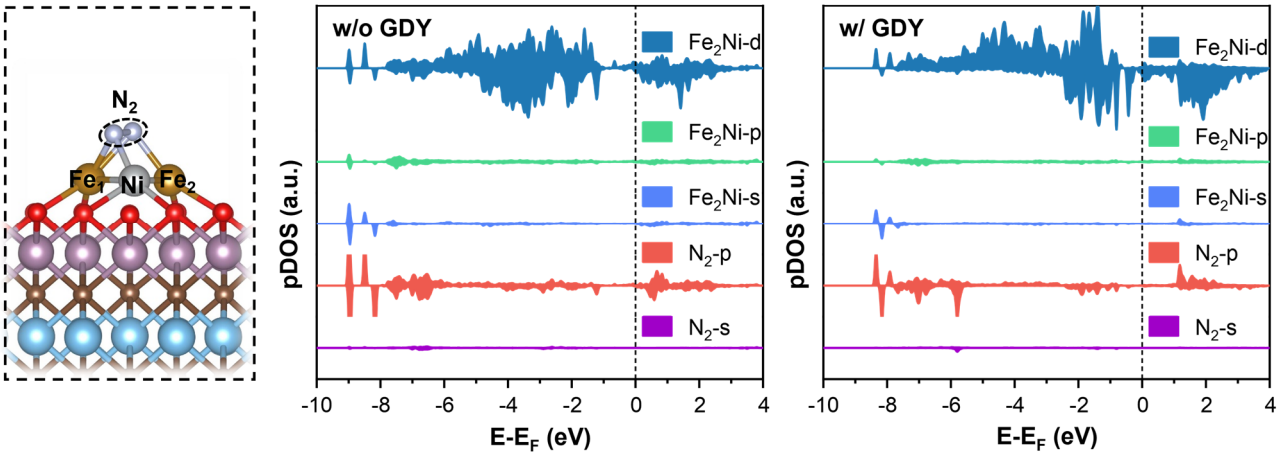

Fig. S8. Projected density of states (pDOS) for N_2 adsorption on $Fe_2Ni/Mo_2TiC_2O_2$ without and with GDY.

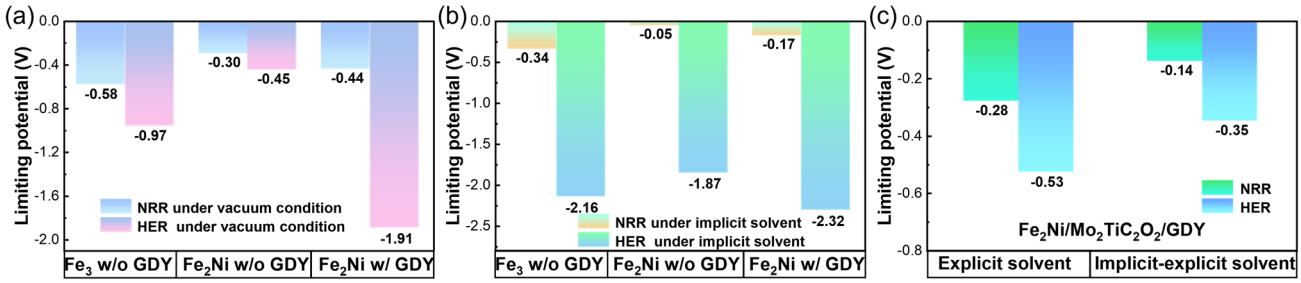

Fig. S9. Limiting potentials for nitrogen reduction reaction (NRR) and hydrogen evolution reaction (HER) on $Fe_3/Mo_2TiC_2O_2$, $Fe_2Ni/Mo_2TiC_2O_2$ and $Fe_2Ni/Mo_2TiC_2O_2$/GDY under vacuum (a), implicit solvent (b), explicit and mixed implicit-explicit solvent conditions (c).

References

1 J. Hafner, J. Comput. Chem., 2008, 29, 2044-2078.
2 J. P. Perdew, K. Burke and M. Ernzerhof, Phys. Rev. Lett., 1996, 77, 3865-3868.
3 S. Grimme, J. Antony, S. Ehrlich and H. Krieg, J. Chem. Phys., 2010, 132, 154104.
4 C. Si, K.-H. Jin, J. Zhou, Z. Sun and F. Liu, Nano Lett., 2016, 16, 6584-6591.
5 D. Xiong, T. Liu, J. Xie, X. Liu and J. Su, J. Colloid Interface Sci., 2025, 685, 998-1007.
6 S. Steinberg and R. Dronskowski, Crystals, 2018, 8.
7 Y. Yao, S. Zhu, H. Wang, H. Li and M. Shao, J. Am. Chem. Soc., 2018, 140, 1496-1501.
8 P. Shu, X. Qi, Q. Peng, Y. Chen, X. Gong, Y. Zhang, F. Ouyang and Z. Sun, Mol. Catal., 2023, 539, 113036.
9 S. Wang, B. Li, L. Li, Z. Tian, Q. Zhang, L. Chen and X. C. Zeng, Nanoscale, 2020, 12, 538-547.
10 X. Zhai, H. Dong, Y. Li, X. Yang, L. Li, J. Yang, Y. Zhang, J. Zhang, H. Yan and G. Ge, J. Colloid Interface Sci., 2022, 605, 897-905.
11 A. Standard, Annual book of ASTM standards, 2008, 12.
12 L. Shulenburger, A. D. Baczewski, Z. Zhu, J. Guan and D. Tomanek, Nano Lett., 2015, 15, 8170-8175.
13 J. Yang, W. Liu, M. Xu, X. Liu, H. Qi, L. Zhang, X. Yang, S. Niu, D. Zhou, Y. Liu, Y. Su, J.-F. Li, Z.-Q. Tian, W. Zhou, A. Wang and T. Zhang, J. Am. Chem. Soc., 2021, 143, 14530-14539.
14 A. Hagopian, M.-L. Doublet, J.-S. Filhol and T. Binninger, J. Chem. Theory Comput., 2022, 18, 1883-1893.
15 J.-C. Liu, F. Luo and J. Li, J. Am. Chem. Soc., 2023, 145, 25264-25273.
16 R. Yu, Z. Liu, D. Legut, J. Sun, Q. Zhang, J. S. Francisco and R. Zhang, ACS Catal., 2024, 14, 10568-10582.
17 K. Mathew, R. Sundararaman, K. Letchworth-Weaver, T. A. Arias and R. G. Hennig, J. Chem. Phys., 2014, 140, 084106.
18 Z. Ma, Y. Luo, P. Wu, J. Zhong, C. Ling, Y. Yu, X. Xia, B. Song, L. Ning and Y. Huang, Adv. Funct. Mater., 2023, 33.
19 H. Xu, D. Cheng, D. Cao and X. C. Zeng, Nat. Catal., 2024, 7, 207-218.